

Two-Layer Stratified Flow past a Valley

RICHARD ROTUNNO

National Center for Atmospheric Research, Boulder, Colorado

MANUELA LEHNER

Department of Atmospheric Sciences, University of Utah, Salt Lake City, Utah

(Manuscript received 29 April 2016, in final form 7 July 2016)

ABSTRACT

Observations and models of nocturnal katabatic winds indicate strong low-level stability with much weaker stability aloft. When such winds encounter an embedded depression in an otherwise smooth sloping plane, the flow responds in a manner that is largely describable by the inviscid fluid dynamics of stratified flow. Building on earlier work, the present study presents a series of numerical simulations based on the simplest nontrivial idealization relevant to the observations: the height-independent flow of a two-layer stratified fluid past a two-dimensional valley. Stratified flow past a valley has received much less attention than the related problem of stratified flow past a hill. Hence, the present paper gives a detailed review of existing theory and fills a few gaps along the way. The theory is used as an interpretive guide to an extensive set of numerical simulations. The solutions exhibit a variety of behaviors that depend on the nondimensional input parameters. These behaviors range from complete flow through the valley to valley-flow stagnation to situations involving internal wave breaking, lee waves, and quasi-stationary waves in the valley. A diagram is presented that organizes the solutions into flow regimes as a function of the nondimensional input parameters.

1. Introduction

This theoretical study is motivated by observations of, and numerical simulations related to, stratified flow over the Arizona Meteor Crater (Lehner et al. 2016a,b). Figure 1 (Lehner et al. 2016a, their Fig. 2) summarizes the major flow features during a downslope-windstorm-type flow with a warm intrusion. As shown by the upstream temperature profile $T(z)$ in Fig. 1b, a very strong ground-based stable layer develops during the night; the gentle slope of the terrain surrounding the crater (Fig. 1a) induces a katabatic slope flow $u(z)$ that encounters the crater. Although these upstream profiles are the result of radiation and turbulence, the numerical simulations in Lehner et al. (2016b) indicate the response of the flow to the presence of the crater can largely be described by the dynamics of inviscid adiabatic stratified flow past a two-dimensional crater, or valley (viscous boundary layer separation and diabatic heating played secondary roles). Motivated by the latter insight, the present paper takes

the idealization of Lehner et al. (2016b) a step further by considering slope-flow-relevant upstream profiles of $T(z)$ and $u(z)$ over level ground containing a valley to study the essentially inviscid, adiabatic flow response.

The general knowledge on stratified flow past a valley is discussed and summarized in Baines (1995, hereafter B95, section 5.14). As described in B95, a basic question regarding such flows is “Under what conditions will air be swept from, or rather stagnate in, the valley?” B95 considers the canonical case of a uniformly stratified (constant Brunt–Väisälä frequency N), constant flow U of infinite depth past a valley of depth H . Under these conditions, B95 asks the reader to imagine two hypothetical evolutions: In the first thought experiment, one pictures an established steady flow (U, N) over level ground that gradually develops a valley [$H = H(t)$, where t is time]. The gradual deepening of the valley allows one to conceive of a succession of steady-state solutions to Long’s equation (Long 1953), which are determined by NH/U ; eventually a threshold would be reached in which the horizontal velocity $u = 0$ at some point in the valley (B95, his Fig. 5.53). Numerical solutions for flow over periodic valleys (Kimura and Manins 1988) suggest that further increases of NH/U lead to

Corresponding author address: Richard Rotunno, National Center for Atmospheric Research, P. O. Box 3000, Boulder, CO 80307.
E-mail: rotunno@ucar.edu

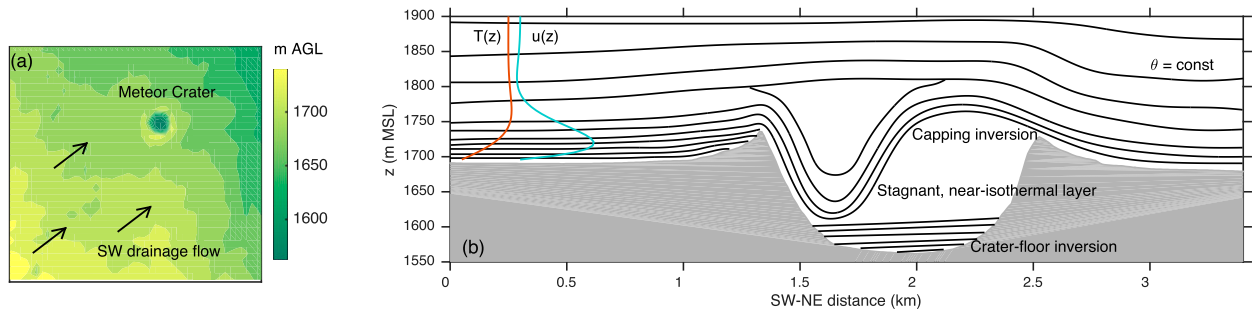


FIG. 1. (a) Schematic diagram of the airflow and (b) thermal structure of flow upstream and in the Arizona Meteor Crater (after Lehner et al. 2016a).

wave breaking, flow deceleration, and eventual flow stagnation within the valley (B95, his Fig. 5.55). In the second thought experiment, B95 imagines an initial state given by a valley filled with stagnant, heavy fluid with constant flow U above [B95, his (5.14.2)]. B95 describes the hypothetical development scenario: “Immediately following the commencement of motion, the fluid in the valley moves downstream so that its upper boundary or “interface” tilts upward in the downstream direction” (p. 337). The buoyancy would then act (on a time scale N^{-1}) to oppose the interface tilt; comparing the buoyancy time scale to the advective time scale (L/U , where L is the valley width), B95 argues that the outcome of the thought experiment is determined by the ratio of time scales and concludes if $NL/U \gg 1$, the heavy fluid will remain in the valley. These arguments will be revisited in light of the present numerical experiments.

In the physical situation of the Meteor Crater there is a gently sloping terrain with an embedded crater; after sunset, surface-based longwave radiational cooling creates a strong low-level stratification and a slope flow. Based on this observed evolution, we imagine an idealization similar to B95’s second scenario, but one in which a preexisting stratification is approximated by two layers, with the first defined by a constant N between the ground and the inversion depth $z = D$ and the second one defined as unstratified for $z > D$. The subsequent slope flow is approximated by the sudden onset of a constant velocity U in the x direction.¹ The physical problem is illustrated in Fig. 2a.

Here we report on a series of numerical experiments based on the initial conditions shown in Fig. 2a. Dimensional analysis indicates the experimental outcomes can depend on at most three nondimensional parameters, which we choose as the nondimensional valley depth and width, NH/U and NL/U , respectively, and the Froude number $F_D = \pi U/2ND$, which gives the ratio of

upstream flow speed to that of the fastest internal gravity wave in the layer D . The present numerical solutions indicate flow stagnation in the valley occurs when both NL/U and $N|H|/U$ are large. In the hydrostatic limit ($NL/U \gg 1$), the main solution dependence is found to be on NH/U and F_D . With $NH/U < -1$, the solutions have some degree of flow stagnation in the valley for any F_D ; in the range $-1 < NH/U < 0$, solutions are found in which there is no stagnation along the valley floor. These solutions take a variety of forms ranging from steady symmetric flow about the valley center (describable by Long’s equation) to internal wave breaking, depending on the combination (F_D , NH/U).

In section 2 we review the basic theory for flows such as the one schematized in Fig. 2. The numerical experiments are described in section 3, and the theoretical constructs reviewed in section 2 are then used in section 4 as a guide to the interpretation of the numerical solutions and the construction of regime diagrams. We summarize the results in section 5.

2. Theory

a. Basic equations

Although the numerical model used in this study solves the fully compressible, variable-density, nonhydrostatic equations of atmospheric motion, in the current application the solutions will be close to those of the shallow, Boussinesq, anelastic equation set of Ogura and Phillips (1962). The equations for momentum, energy, and continuity are, respectively,

$$\frac{D\mathbf{u}}{Dt} = -\nabla(c_p\theta_0\Pi') + b\mathbf{k}, \quad (1a)$$

$$\frac{Db}{Dt} = -N^2w, \quad \text{and} \quad (1b)$$

$$\partial_x u + \partial_z w = 0, \quad (1c)$$

with $D/Dt \equiv \partial_t + u\partial_x + w\partial_z$, where $\mathbf{u} = u\mathbf{i} + w\mathbf{k}$ is the two-dimensional (x - z) velocity; $b = g\theta'/\theta_0$ is the

¹ Or, alternatively, the ground with embedded valley suddenly accelerates in the x direction to the speed $-U$.

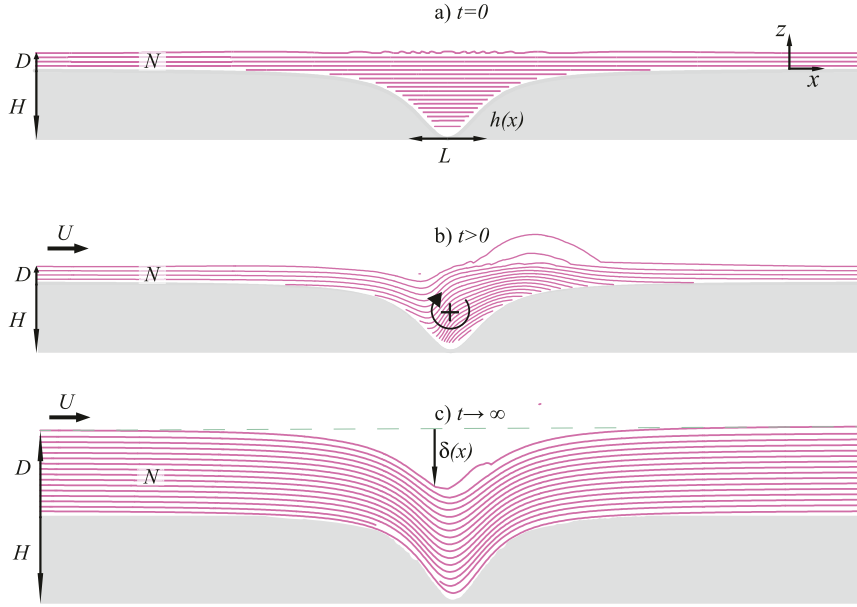


FIG. 2. Schematic diagram of the flow studied here as visualized by the isentropes (red contour lines) for three situations: (a) the initial state before motion is impulsively started; (b) the initial motion U creates a potential flow that attempts to displace downstream the initial cold air in the valley, and the tilted isentropes create positive y -directed vorticity η ; and (c) an example of a steady-state solution in which the cold air has been swept away and flow symmetric about the valley center remains. In (c), the displacement $\delta(x)$ of the uppermost isentrope is indicated.

buoyancy; and $c_p \theta_0 \Pi'$ is the pressure variable ($\text{m}^2 \text{s}^{-2}$). The potential temperature $\theta = \theta_0 + \bar{\theta}(z) + \theta'(x, z, t)$, where θ_0 is constant, $N^2 = g\theta_0^{-1} d\bar{\theta}/dz$, and g is the acceleration due to gravity. The quantity $\Pi = (p/p_s)^{R/c_p} = \bar{\Pi}(z) + \Pi'$, where Π' is the perturbation away from the hydrostatic base state $\bar{\Pi}(z)$, p is the pressure, p_s is the base-state surface pressure, c_p is the specific heat at constant pressure, and R is the gas constant for dry air.

b. Linear theory

First, the linear theory of motion for the upstream flow is reviewed following B95 (chapter 4.2). Equations (1a)–(1c) are linearized by letting $D/Dt \simeq \partial_t + U\partial_x$, where U is taken as a constant for simplicity. With the definition of the streamfunction ψ [where $(u, w) = (\partial_z \psi, -\partial_x \psi)$], the governing equations may be combined into the single equation:

$$(\partial_t + U\partial_x)^2 (\partial_{xx} + \partial_{zz})\psi + N^2 \psi_{xx} = 0. \quad (2)$$

The particular case of a constant- N , finite-depth layer $D + \delta(x, t)$, where $\delta \ll D$, describes the flow upstream of the valley (Fig. 2). In this case, the solution to (2) for a disturbance of wavenumber k in the layer $0 \leq z \leq D$ is

$$\psi(x, z, t) = \sin m z e^{ik(x-ct)}, \quad c = U \pm \frac{N}{(k^2 + m^2)^{1/2}}, \quad (3)$$

where m is the eigenvalue (vertical wavenumber), given by the solution to

$$k \sin m D + m \cos m D = 0. \quad (4)$$

Condition (4) guarantees the continuity of ψ and $\partial_z \psi$ at $z = D$ with the solution for $z \geq D$, which is $\psi(x, z, t) = \sin m D e^{-k(z-D)} e^{ik(x-ct)}$. The group velocity $c_g = \partial_k(kc)$ can be derived from (3) as

$$c_g = U \pm \frac{Nm^2}{(k^2 + m^2)^{3/2}} \quad (5)$$

(B95, p. 176). The second term on the rhs of (5) is the intrinsic group velocity. Inspection of (5) indicates that the fastest intrinsic group velocity occurs in the long-wave limit ($k^2 \ll m^2$), in which

$$c_g \rightarrow c = U \pm \frac{N}{m}. \quad (6)$$

From (6), the fastest intrinsic group and phase velocities occur for the smallest m , which (4) in the longwave limit gives as $m = \pi/2D$. Hence the condition for zero upstream propagation of wave energy is $c_g = 0$ or

$$\frac{\pi U}{2ND} = F_D = 1, \quad (7)$$

at which point the flow is said to be *critical*; accordingly, a flow is said to be *supercritical* for $F_D > 1$ and *subcritical* for $F_D < 1$.

When the lower boundary has the topographical feature $h(x)$, the lower boundary condition is $\psi[x, z = h(x)] = 0$, which is linearized as $\psi(x, 0) = -Uh(x)$. The standard analysis (B95, see the appendix) considers the Fourier transform in x of the steady version of (2); the solution in the present case is

$$\hat{\psi}(k, z) = -U\hat{h}(k) \frac{k \sin m(D - z) + m \cos m(D - z)}{k \sin mD + m \cos mD}, \quad (8)$$

where a hat denotes the Fourier transform. In this equation, k is the continuously varying transform parameter, and $m = \sqrt{N^2/U^2 - k^2}$ for $0 < |k| < N/U$; for $|k| > N/U$, $m = \sqrt{k^2 - N^2/U^2}$ and $\sin(\dots)$ and $\cos(\dots)$ are replaced by $\sinh(\dots)$ and $\cosh(\dots)$, respectively, in (8). If the upstream flow is subcritical ($F_D < 1$), it can be shown there exist values of k that bring the denominator of (8) to zero; upon taking the inverse Fourier transform of (8), the zeroes in the denominator correspond to lee waves in the physical (x) coordinate.

c. Nonlinear theory: Long’s equation

The steady form of the two-dimensional nonlinear equations in (1a)–(1c) can be written as

$$\eta = \frac{dE}{d\psi} + z \frac{db}{d\psi}, \quad (9)$$

where $\eta = \partial_z u - \partial_x w = \nabla^2 \psi$ and $E = (u^2 + w^2)/2 + c_p \theta_0 \Pi' - bz$; (9) is known as Long’s equation and is described in various texts (e.g., Yih 1965, chapter 3). In the present case with upstream profiles given by constant U over the entire fluid depth and constant N over the finite-depth D , $E = E_0 - (1/2)(N\psi/U)^2$ and $b = b_0 + N^2\psi/U$ for $0 \leq \psi \leq UD$ and $E = E_0 - (1/2)(ND)^2$, and $b = b_0 + N^2D$ for $UD \leq \psi$, where E_0 and b_0 are constants; substituting these into the rhs of (9) and using the definition of η gives

$$\nabla^2 \psi = \begin{cases} -\frac{N^2}{U^2} \psi + \frac{N^2}{U} z & \text{for } 0 \leq \psi \leq UD \\ 0 & \text{for } UD \leq \psi. \end{cases} \quad (10)$$

The solution to (10) with boundary conditions $\psi[x, z = h(x)] = 0$ and $|\psi| < \infty$ for $z \rightarrow \infty$ provides the fully nonlinear steady-state solution over the valley. The free boundary $D + \delta(x, z)$ (see, for example, Fig. 2c) is located where $\psi = UD$ and must be solved for to insure that all boundary conditions are satisfied. Solutions to Long’s equation are valid so long as no closed streamlines appear [i.e., all streamlines are assumed to originate upstream with known values of $E(\psi)$ and $b(\psi)$]. Overturning

streamlines in the solutions indicate the possibility of static instability, which affects their realizability.

For the present purposes, it suffices to take advantage of the significant simplification attaching to the assumption of hydrostatic flow in which $\nabla^2 \psi \simeq \partial_{zz} \psi$. The solution to (10) in this case is

$$\psi(x, z) = \begin{cases} Uz - U\delta \cos \frac{N}{U}(D + \delta - z) & \text{for } 0 \leq \psi \leq UD \\ Uz - U\delta & \text{for } UD \leq \psi; \end{cases} \quad (11)$$

the free boundary $\delta(x)$ is obtained by application of the lower boundary condition $\psi = 0$ at $z = h(x)$ in (11), which gives the equation

$$h = \delta \cos \frac{N}{U}(D + \delta - h); \quad (12)$$

with h given, δ can be found through numerical techniques. This solution in (11) and (12) was first derived by Smith (1985, hereafter S85) in his explanation of downslope windstorms and further explored in Durran and Klemp (1987) and Baines and Granek (1990). Here we focus on solution features for the case of a valley ($h < 0$).

Figure 3 is a modified version of S85’s Fig. 2 in which (12) is solved for $N\delta/U$ as a function of Nh/U with $ND/U = n\pi/6$ ($n = 0, 1, 2, \dots$) specified as a parameter. Equation (7) indicates $ND/U = \pi/2F_D$, implying $F_D = 3/n$. We have kept only the solution curves that pass through the origin as the idea is to follow a curve into the valley starting from $h = 0$. For $n < 3$, the upstream flow is supercritical; following any one of the curves $n = 0, 1$, and 2 from the initial state $(h, \delta) = (0, 0)$ into, then back out of, the valley shows that the flow returns to its original state. On the other hand, for $n > 3$, the upstream flow is subcritical; for cases $n = 4$ –8 (or more generally, $1 > F_D > 1/3$), the solution curves show δ increasing and allow for the possibility of the flow not returning to its original state, for, if the flow reaches the minimum h , it may continue out of the valley following the upper branch with continued increasing δ . The case $n = 3$ is exactly critical and one can surmise that a flow would follow either the subcritical or the supercritical branch depending on any slight variation in the upstream condition, but, strictly speaking, the solution behavior is indeterminate. The case $n = 9$ is also a special case in that there are no solution curves passing through the origin for $h < 0$. We will return below to the case $n = 10$.

Durran and Klemp (1987) showed (12) can be used to derive

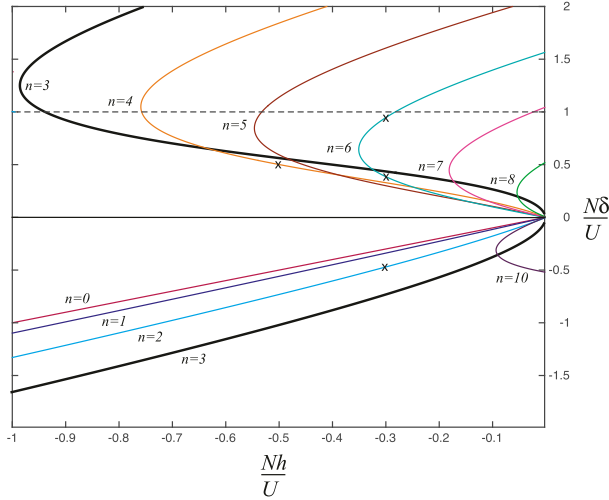


FIG. 3. Solution of (12), following Fig. 2 of S85 but showing a wider range of Nh/U and only the curves that pass through the origin. We follow S85 and plot solutions for $ND/U = n\pi/6$, indicating the Froude number $F_D = (\pi U/2ND) = 3/n$, which defines flow criticality ($F_D = 1$) as the case $n = 3$. Solutions above the horizontal dashed line exhibit reversed flow and thus are technically invalid.

$$\partial_x h = (1 - \mathcal{F}^{-2})\partial_x \delta, \tag{13}$$

where

$$\mathcal{F}^{-2} = \frac{1 - \text{cos}l\phi}{1 - l\delta \text{sin}l\phi}, \tag{14}$$

with $\phi = (D + \delta - h)$ and $l = N/U$. Equation (13) has a form analogous to the equivalent expression in single-layer shallow-water theory in which the height of the displacement of the free surface (analogous to δ) is related to the topographical variation $h(x)$, and the local Froude number \mathcal{F} is analogous to the shallow-water version $F = u^2/g\phi$, where u is the layer velocity. For the supercritical case, Fig. 3 shows $h \propto \delta$, which implies $\mathcal{F} > 1$ for all x including the valley bottom, where $\partial_x h = 0$, and by (13), $\partial_x \delta = 0$, and thus the solution is symmetric [$\delta(x = -\infty) = \delta(x = +\infty)$]. For the subcritical cases, Fig. 3 together with (13) shows that $\mathcal{F} = 1$ at the minimum h since $\partial_x \delta \neq 0$ at that point. Equation (16) of Durran and Klemp (1987) shows that $\partial_x \delta > 0$ at the valley center, and therefore the solution is not symmetric [$\delta(x = -\infty) \neq \delta(x = +\infty)$]. As an aside, we note that the actual shallow-water equations have no critical-flow transitions for either subcritical or supercritical flow approaching a valley (B95, p. 39).

Figure 4 shows example solutions $u(z)$ for the points marked by the crosses on the curves $n = 2, 4$, and 6 in Fig. 3. In the supercritical case (Fig. 4a), the layer thins

and the flow accelerates throughout. For the subcritical cases (Figs. 4b–d), the layer thickens and continuity requires a net flow deceleration. The case $n = 4$ (Fig. 4b) shows the entire layer decelerated. In contrast, the two cases with $n = 6$ (Figs. 4c,d) indicate flow acceleration at the surface with deceleration at higher levels. Using (11), it is a simple exercise to show that the minimum velocity in the lower layer reaches zero when $N\delta/U = 1$, independent of Nh/U ; this limit is shown as the dashed line in Fig. 3. Reversed flow (or, equivalently, $\partial_z b < 0$) occurs for solutions with $N\delta/U > 1$, and the solutions are likely statically unstable.

Figure 5, also based on (12), is a partial reconstruction of Fig. 4 of Baines and Granek (1990), in which solution regimes are identified as a function of F_D and H/D (the nondimensional valley bottom). For $F_D > 1$ (or $n < 3$ in Fig. 3), there are no critical-flow transitions for any H/D . However, for $1/3 < F_D < 1$ ($9 > n > 3$ in Fig. 3), solutions are possible for H/D in the region bounded on the left by the solid blue line, which is the locus of points at which h is a minimum in Fig. 3, or by (13), $\mathcal{F} = 1$; at this point, a critical-flow transition is possible as discussed above. For $F_D < 1/3$, Fig. 4 of Baines and Granek (1990) has increasingly complex states described; for simplicity, Fig. 5 shows only the states that lie in the interval $1/5 < F_D < 1/3$. In this region, the solutions indicate flow acceleration ($\delta < 0$) consistent with the $n = 10$ curve in Fig. 3; however, at $F_D \lesssim 0.26$, the solutions have regions of overturning streamlines and are susceptible to instability. Finally, the red line is where $NH/U = -1$ [$F_D = -(\pi/2)H/D$]. Solutions to the left of this line ($NH/U < -1$) are expected to have flow stagnation in the valley based on heuristic arguments, an example of which is given next.

d. Nonlinear theory: Heuristic theory for valley-flow stagnation

We pursue the thought experiment in the framework of B95 (p. 337). Shortly after the initial impulsive acceleration, the terrain-following potential flow acts to displace the air in the valley downstream, as illustrated in Fig. 2b. Baroclinic effects start to produce the y -directed vorticity η according to

$$\frac{D\eta}{Dt} = -\partial_x b \tag{15}$$

[in consequence of (1a) and (1c)]. Based on the initial tendency of the flow to scour out the cold air in the valley shown in Fig. 2b, we estimate $-\partial_x b \simeq -[(b_0 + N^2 H) - b_0]/L = -N^2 H/L$. The time to advect the cold air out of the valley is $\simeq L/U$, and using these we have the following from (15):

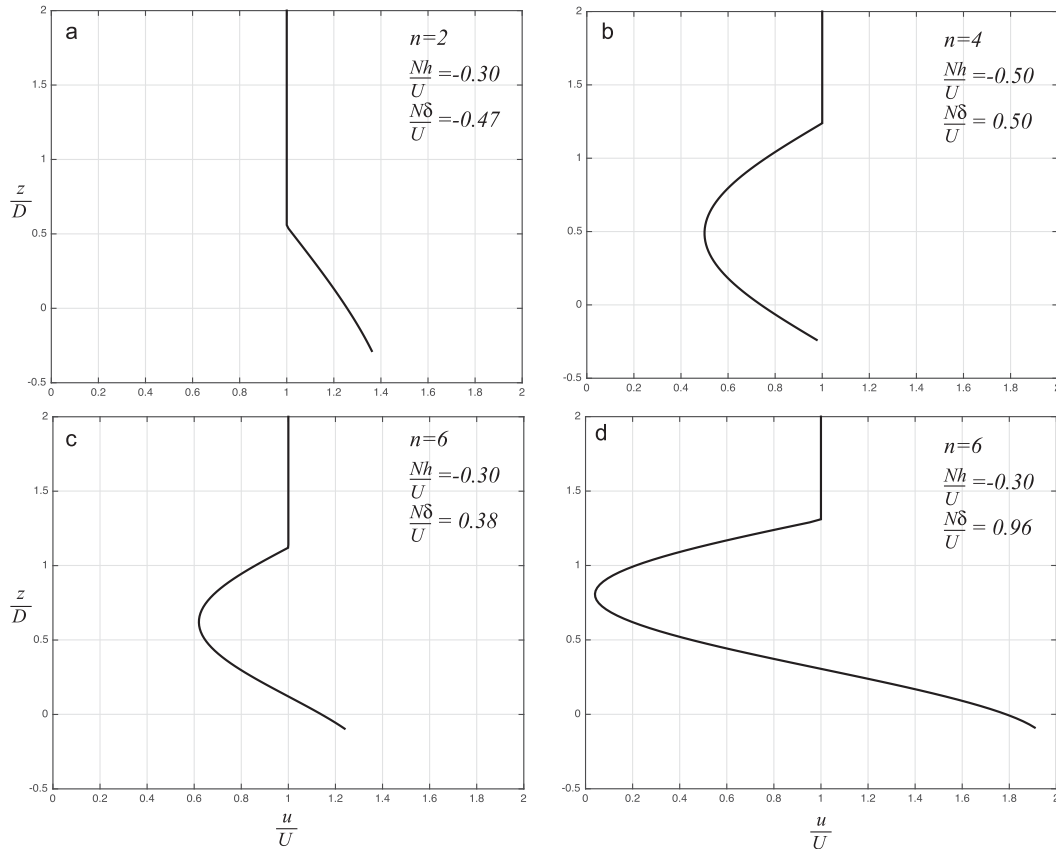


FIG. 4. Examples of the $u(z)$ for the solutions indicated by the crosses in Fig. 3: (a) supercritical (lower layer thin, flow accelerates throughout the layer); (b) subcritical (lower layer thickens, flow decelerates throughout the layer); and (c),(d) subcritical (lower layer thickens, flow accelerates along the surface, decelerates near midlayer depth). One may think of (c) as the flow descending into the valley and (d) as the flow ascending out of the valley.

$$\frac{U}{L}\eta \simeq -N^2\frac{H}{L}, \quad (16)$$

which implies $\eta > 0$ since $H < 0$. Figure 2 illustrates the initial production of $\eta > 0$, which induces low-level motion in opposition to the mean flow.

To estimate $\eta = \partial_z u - \partial_x w$, we look for the rotary motion in the valley (Fig. 2b) that brings u to zero on the valley floor; hence, $\partial_z u \simeq U/|H|$ for the first term of η ; for the second term, the imagined rotary motion is taken to be the exact opposite of the initial flow: namely, $w \simeq -2UH/L > 0$ for $x < 0$ (valley center) and $w \simeq 2UH/L < 0$ for $x > 0$ so that $-\partial_x w \simeq -4UH/L^2$ at $x = 0$; substitution into (16) gives the condition for stagnation as

$$\frac{N|H|}{U} \frac{1}{\sqrt{1 + (2H/L)^2}} = 1. \quad (17)$$

If $(2H/L)^2 \ll 1$, we recover $N|H|/U = 1$, the condition corresponding to the red line in Fig. 5. In the opposite

limit $(2H/L)^2 \gg 1$, the condition for stagnation is $NL/2U = 1$, similar to the result stated in B95 (p. 339). Using (17) and adjusting the sign, one can show

$$F_D = -\frac{\pi}{2} \frac{H}{D} \frac{1}{\sqrt{1 + (2H/L)^2}}, \quad (18)$$

which implies that nonhydrostatic effects act against flow stagnation since finite H/L reduces the slope (less negative) of the red line in Fig. 5.

3. Numerical experiments

The present numerical experiments are carried out with Cloud Model 1 (CM1; Bryan and Fritsch 2002). Two-dimensional (y independent) flows are simulated on a domain that is 45 km in the x (along flow) direction and 6 km in the z (vertical) direction with the valley centered in the domain. In the x direction, we use a stretched grid that ranges in grid size from 30 m in the center to 150 m near the boundaries. The

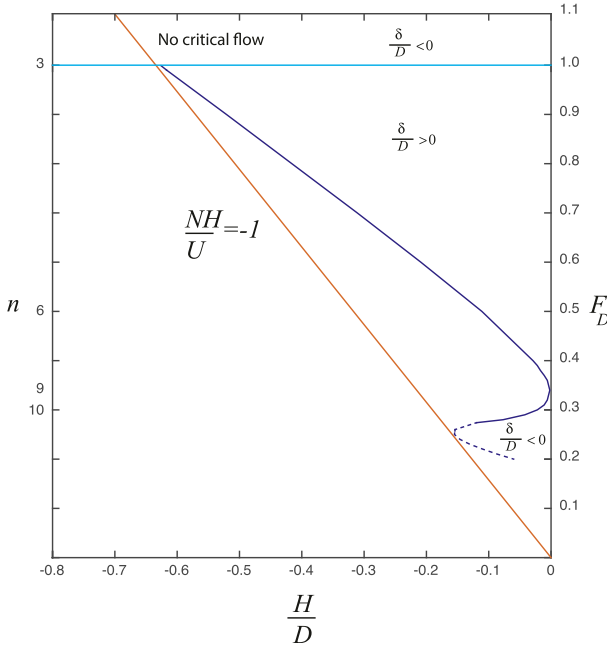


FIG. 5. Solution of (12), following Fig. 4 of Baines and Graneek (1990), but only for $F_D > 0.2$ and with the n of Fig. 3 given on the left-side ordinate. For $F_D > 1$, the flow is supercritical without the possibility of critical-flow transition ($0 \leq n < 3$ in Fig. 3). For $1 > F_D \geq 1/3$, the blue curve represents the minimum h corresponding to the solutions $3 < n \leq 9$ in Fig. 3. Solutions are possible for $F_D < 1/3$ ($n > 9$), but, below a certain value, they exhibit static instability (dashed line). Parameters in the space to the left of the red line [$F_D = -(\pi/2)H/D$] have valley-flow stagnation according to heuristic arguments.

horizontal grid spacing is constant in the innermost 3000 m ($\Delta x|_i = 30$ m), beyond which it is stretched to $\Delta x|_o = 150$ m at the lateral boundaries, with $\Delta x|_l = \Delta x|_i + 2(l-1)(\Delta x|_m - \Delta x|_i)/(n-1)$, where l is the grid point index outside of the constant grid-spacing region, n ($=232$) is the number of grid points in the stretched part, and $\Delta x|_m = 0.5(\Delta x|_i + \Delta x|_o)$. We also employ grid stretching in the vertical that varies from a grid size of 2 m near the surface to 150 m above approximately 3 km. The vertical grid spacing is constant below $z_B = 30$ m ($\Delta z|_B = 2$ m) and above $z_T = 3070$ m ($\Delta z|_T = 150$ m), with a total domain depth of 6070 m. The vertical grid spacing in the stretched middle layer is $\Delta z|_k = \Delta z|_B + 2(k-1)(\Delta z|_m - \Delta z|_B)/(n_M - 1)$, where k is the grid-level index in the stretched layer, n_M ($=15$) and n_B ($=40$) are the number of grid levels in the middle and bottom layers, respectively, and $\Delta z|_m = 0.5(\Delta z|_T + \Delta z|_B)$.

Open boundary conditions are applied at the upwind and downwind boundaries, respectively. The valley is represented by a Witch of Agnesi profile embedded in a plain given by

$$h(x) = \frac{H}{1 + (2x/L)^2}, \quad (19)$$

where H (<0) is the valley depth and $L/2$ is the valley half-width. A Rayleigh damping layer is applied above $z = 4$ km. Coefficients of viscosity and heat transfer are set to zero. No planetary boundary layer (PBL) or other turbulence parameterization is used.

The simulations are initialized with a constant wind speed U throughout the domain and constant N within the lowest layer below $z = D$ and a weakly stratified layer above ($N^2 = 10^{-5} \text{ s}^{-2}$). The height D is defined with respect to the top of the basin at $z = 0$. The simulations are summarized in Table 1; all are done with valley depths of $H = -10, -20, -50, -100, -150$, and -200 m and a valley width $L = 500$ m. Several simulations were repeated with $L = 250, 1000, 2000$, and 4000 m. The simulations are run for 1 h with a time step of 0.1 s, and the analysis is based on 5-min-averaged output. CM1 uses a Runge–Kutta time integration method, and a fifth-order-weighted essentially non-oscillatory (WENO) advection scheme was used in this study. The integration is horizontally explicit and vertically implicit. We used an acoustic time step of $0.1/8 \text{ s} (=0.0125 \text{ s})$.

As described above, the flow is impulsively started, and, given the effective incompressibility of this flow and finite time (N^{-1}) for baroclinic effects to have an effect, the initial flow is a terrain-following potential flow. The subsequent displacement of the isentropes (as in Fig. 2b) initiates the evolution toward the steady-state solution (e.g., Fig. 2c), which depends on the input parameters U, N, H, D , and L . To provide the context for our interpretation of the numerical solutions, the next section briefly reviews the relevant theoretical concepts.

4. Results and discussion

We have examined each numerical solution in the present set of experiments (Table 1) and subjectively identified nine categories. Examples of the various solution types are shown in Fig. 6, and every solution in the present series is represented in Fig. 7 according to its category. While some of these flows can be located on the Long's solution diagram shown in Fig. 3, most fall outside the plotting coordinates. For this reason, we use a regime diagram based on Fig. 5 that can accommodate a wider range in parameter space. In the following, each solution in Fig. 6 is described in relation to the theoretical results reviewed in section 2.

Figure 6a is an example of the supercritical-flow solution (open red triangle in Fig. 7) found in Long's equation (cf. Fig. 4a). The position of this flow on Fig. 3

TABLE 1. Parameter values for the numerical simulations: (left)–(right) the Brunt–Väisälä frequency N (s^{-1}), wind speed U (m s^{-1}), depth of the inversion layer D (m), maximum valley depth H (m), and valley width L (m), as well as nondimensional numbers F_D , $-NH/U$, $-H/D$, and NL/U . Several simulations were run with multiple valley widths $L = 250 \times 2^j$ m, where $j = 0, 1, 2, 3$, and 4. In all cases $\theta_0 = 290$ K in the calculation of N .

N	U	D	$-H$	L	F_D	$-NH/U$	$-H/D$	NL/U	N	U	D	$-H$	L	F_D	$-NH/U$	$-H/D$	NL/U
0.028	5.0	400	10	500	0.70	0.06	0.03	2.8	0.056	10.0	300	20	500	0.93	0.11	0.07	2.8
0.028	5.0	400	20	500	0.70	0.11	0.05	2.8	0.056	10.0	300	50	500	0.93	0.28	0.17	2.8
0.028	5.0	400	50	500	0.70	0.28	0.13	2.8	0.056	10.0	300	100	500	0.93	0.56	0.33	2.8
0.028	5.0	400	100	500	0.70	0.56	0.25	2.8	0.056	10.0	300	150	500	0.93	0.84	0.50	2.8
0.028	5.0	400	150	500	0.70	0.84	0.38	2.8	0.056	10.0	300	200	500	0.93	1.12	0.67	2.8
0.028	5.0	400	200	500	0.70	1.12	0.50	2.8	0.070	1.0	50	10	500	0.45	0.70	0.20	35.0
0.056	2.5	50	10	250×2^j	1.40	0.22	0.20	5.6×2^j	0.070	1.0	50	20	500	0.45	1.40	0.40	35.0
0.056	2.5	50	20	250×2^j	1.40	0.45	0.40	5.6×2^j	0.070	1.0	50	50	500	0.45	3.50	1.00	35.0
0.056	2.5	50	50	250×2^j	1.40	1.12	1.00	5.6×2^j	0.070	1.0	50	100	500	0.45	7.00	2.00	35.0
0.056	2.5	50	100	250×2^j	1.40	2.24	2.00	5.6×2^j	0.070	2.5	50	10	250×2^j	1.12	0.28	0.20	7.0×2^j
0.056	1.0	75	10	500	0.37	0.56	0.13	28.0	0.070	2.5	50	20	250×2^j	1.12	0.56	0.40	7.0×2^j
0.056	1.0	75	20	500	0.37	1.12	0.27	28.0	0.070	2.5	50	50	250×2^j	1.12	1.40	1.00	7.0×2^j
0.056	1.0	75	50	500	0.37	2.80	0.67	28.0	0.070	2.5	50	100	250×2^j	1.12	2.80	2.00	7.0×2^j
0.056	1.0	75	100	500	0.37	5.60	1.33	28.0	0.070	5.0	50	10	250×2^j	2.24	0.14	0.20	3.5×2^j
0.056	1.0	75	150	500	0.37	8.40	2.00	28.0	0.070	5.0	50	20	250×2^j	2.24	0.28	0.40	3.5×2^j
0.056	1.0	100	10	250×2^j	0.28	0.56	0.10	14.0×2^j	0.070	5.0	50	50	250×2^j	2.24	0.70	1.00	3.5×2^j
0.056	1.0	100	20	250×2^j	0.28	1.12	0.20	14.0×2^j	0.070	5.0	50	100	250×2^j	2.24	1.40	2.00	3.5×2^j
0.056	1.0	100	50	250×2^j	0.28	2.80	0.50	14.0×2^j	0.070	1.0	90	10	500	0.25	0.70	0.11	35.0
0.056	1.0	100	100	250×2^j	0.28	5.60	1.00	14.0×2^j	0.070	1.0	90	20	500	0.25	1.40	0.22	35.0
0.056	1.0	100	150	250×2^j	0.28	8.40	1.50	14.0×2^j	0.070	1.0	90	50	500	0.25	3.50	0.56	35.0
0.056	1.0	100	200	250×2^j	0.28	11.20	2.00	14.0×2^j	0.070	1.0	90	100	500	0.25	7.00	1.11	35.0
0.056	2.5	100	10	250×2^j	0.70	0.22	0.10	5.6×2^j	0.070	1.0	90	150	500	0.25	10.50	1.67	35.0
0.056	2.5	100	20	250×2^j	0.70	0.45	0.20	5.6×2^j	0.070	5.0	100	10	250×2^j	1.12	0.14	0.10	3.5×2^j
0.056	2.5	100	50	250×2^j	0.70	1.12	0.50	5.6×2^j	0.070	5.0	100	20	250×2^j	1.12	0.28	0.20	3.5×2^j
0.056	2.5	100	100	250×2^j	0.70	2.24	1.00	5.6×2^j	0.070	5.0	100	50	250×2^j	1.12	0.70	0.50	3.5×2^j
0.056	2.5	100	150	250×2^j	0.70	3.36	1.50	5.6×2^j	0.070	5.0	100	100	250×2^j	1.12	1.40	1.00	3.5×2^j
0.056	2.5	100	200	250×2^j	0.70	4.48	2.00	5.6×2^j	0.070	5.0	100	150	250×2^j	1.12	2.10	1.50	3.5×2^j
0.056	5.0	100	10	250×2^j	1.40	0.11	0.10	2.8×2^j	0.070	5.0	100	200	250×2^j	1.12	2.80	2.00	3.5×2^j
0.056	5.0	100	20	250×2^j	1.40	0.22	0.20	2.8×2^j	0.070	10.0	100	10	500	2.24	0.07	0.10	3.5
0.056	5.0	100	50	250×2^j	1.40	0.56	0.50	2.8×2^j	0.070	10.0	100	20	500	2.24	0.14	0.20	3.5
0.056	5.0	100	100	250×2^j	1.40	1.12	1.00	2.8×2^j	0.070	10.0	100	50	500	2.24	0.35	0.50	3.5
0.056	5.0	100	150	250×2^j	1.40	1.68	1.50	2.8×2^j	0.070	10.0	100	100	500	2.24	0.70	1.00	3.5
0.056	5.0	100	200	250×2^j	1.40	2.24	2.00	2.8×2^j	0.070	10.0	100	150	500	2.24	1.05	1.50	3.5
0.056	5.0	140	10	500	1.00	0.11	0.07	5.6	0.070	10.0	100	200	500	2.24	1.40	2.00	3.5
0.056	5.0	140	20	500	1.00	0.22	0.14	5.6	0.070	5.0	113	10	500	0.99	0.14	0.09	7.0
0.056	5.0	140	50	500	1.00	0.56	0.36	5.6	0.070	5.0	113	20	500	0.99	0.28	0.18	7.0
0.056	5.0	140	100	500	1.00	1.12	0.71	5.6	0.070	5.0	113	50	500	0.99	0.70	0.44	7.0
0.056	5.0	140	150	500	1.00	1.68	1.07	5.6	0.070	5.0	113	100	500	0.99	1.40	0.88	7.0
0.056	5.0	140	200	500	1.00	2.24	1.43	5.6	0.070	5.0	113	150	500	0.99	2.10	1.33	7.0
0.056	5.0	150	10	500	0.93	0.11	0.07	5.6	0.070	5.0	113	200	500	0.99	2.80	1.77	7.0
0.056	5.0	150	20	500	0.93	0.22	0.13	5.6	0.070	5.0	200	10	500	0.56	0.14	0.05	7.0
0.056	5.0	150	50	500	0.93	0.56	0.33	5.6	0.070	5.0	200	20	500	0.56	0.28	0.10	7.0
0.056	5.0	150	100	500	0.93	1.12	0.67	5.6	0.070	5.0	200	50	500	0.56	0.70	0.25	7.0
0.056	5.0	150	150	500	0.93	1.68	1.00	5.6	0.070	5.0	200	100	500	0.56	1.40	0.50	7.0
0.056	5.0	150	200	500	0.93	2.24	1.33	5.6	0.070	5.0	200	150	500	0.56	2.10	0.75	7.0
0.056	5.0	200	10	250×2^j	0.70	0.11	0.05	2.8×2^j	0.070	5.0	300	10	500	0.37	0.14	0.03	7.0
0.056	5.0	200	20	250×2^j	0.70	0.22	0.10	2.8×2^j	0.070	5.0	300	20	500	0.37	0.28	0.07	7.0
0.056	5.0	200	50	250×2^j	0.70	0.56	0.25	2.8×2^j	0.070	5.0	300	50	500	0.37	0.70	0.17	7.0
0.056	5.0	200	100	250×2^j	0.70	1.12	0.50	2.8×2^j	0.100	5.0	50	10	500	1.57	0.20	0.20	10.0
0.056	5.0	200	150	250×2^j	0.70	1.68	0.75	2.8×2^j	0.100	5.0	50	20	500	1.57	0.40	0.40	10.0
0.056	5.0	200	200	250×2^j	0.70	2.24	1.00	2.8×2^j	0.100	5.0	50	50	500	1.57	1.00	1.00	10.0
0.056	5.0	300	10	250×2^j	0.47	0.11	0.03	2.8×2^j	0.100	5.0	50	100	500	1.57	2.00	2.00	10.0
0.056	5.0	300	20	250×2^j	0.47	0.22	0.07	2.8×2^j	0.100	5.0	100	10	500	0.79	0.20	0.10	10.0
0.056	5.0	300	50	250×2^j	0.47	0.56	0.17	2.8×2^j	0.100	5.0	100	20	500	0.79	0.40	0.20	10.0

TABLE 1. (Continued)

N	U	D	$-H$	L	F_D	$-\frac{NH}{U}$	$-\frac{H}{D}$	$\frac{NL}{U}$	N	U	D	$-H$	L	F_D	$-\frac{NH}{U}$	$-\frac{H}{D}$	$\frac{NL}{U}$
0.056	5.0	300	100	250×2^j	0.47	1.12	0.33	2.8×2^j	0.100	5.0	100	50	500	0.79	1.00	0.50	10.0
0.056	5.0	300	150	250×2^j	0.47	1.68	0.50	2.8×2^j	0.100	5.0	100	100	500	0.79	2.00	1.00	10.0
0.056	5.0	300	200	250×2^j	0.47	2.24	0.67	2.8×2^j	0.100	5.0	100	150	500	0.79	3.00	1.50	10.0
0.056	10.0	300	10	500	0.93	0.06	0.03	2.8	0.100	5.0	100	200	500	0.79	4.00	1.00	10.0

can be located by the indicated values of $n = 1.3$ and $NH/U = -0.28$ and in Fig. 7c. Figure 6b is an example of a flow with supercritical conditions upstream, but with $NH/U < -1$ (Fig. 7c); there is flow stagnation in the valley (filled red triangle in Fig. 7). This flow appears to be most similar to those observed in the Meteor Crater Experiment (cf. Fig. 1).

Figure 6c is an example of the subcritical-flow solution found in Long’s equation (cf. Fig. 4c; open black circle with cross in Fig. 7). The position of this flow on Fig. 3 can be located by the indicated values of $n = 6.4$ and $NH/U = -0.22$ and in Fig. 7c. Going to a deeper valley for the same F_D and NL/U , Fig. 6d indicates strongly accelerated flow at the valley bottom with nearly zero flow just above the midlayer depth (open black circle with cross in Fig. 7), similar to the Long’s solution shown in Fig. 4d. In this case, one can use Fig. 3 to speculate that valleys as deep as (or deeper than) the minimum h for the same n can follow the upper branch of the solution curves in Fig. 3 and thus may have flow reversal. This interpretation is consistent with the fact that the position of the solution in Fig. 7c is to the right of the red stagnation line but to the left of the allowable Long’s solution curve (blue line).

Figure 6e should have been an example of the subcritical-flow solution found in Long’s equation (Figs. 4b and 7c; open black triangle in Fig. 7). Unexpectedly, however, the solution exhibits a number of short waves that appear to be generated on the downwind valley wall and propagate slowly upstream. A possible explanation is that the significant deceleration over the entire lower layer implied in Long’s theory (Fig. 4b) leads to a situation of nearly stagnant flow in the valley, putting the flow at the threshold between flow sweeping out of, or stagnating in, the valley. The shorter wavelength of these waves also implies slower intrinsic wave speeds by (3). Going to a deeper valley for the same (subcritical) F_D and NL/U makes $NH/U = -2.24$ and puts the solution to the left of the stagnation line in Fig. 7c. The corresponding Fig. 6f indicates a layer of stagnant flow in the valley with upstream-propagating short waves now generated on the leading edge of the stagnant cold air in the valley (filled black triangle in Fig. 7).

Figure 6g is an example of a valley flow with standing lee waves (open black circle in Fig. 7). In comparison with Fig. 6c, all the parameters are the same, save for L , which is reduced by a factor of 4 (Fig. 7a), and lee waves become a more prominent feature of the solution.

Figure 6h is typical of solutions with nearly total valley-flow stagnation (filled green diamond in Fig. 7), as its position on Fig. 7d is well to the left of the stagnation threshold line. The flow above the valley is disorganized and weak.

Figure 6i is an example of the nonhydrostatic effect anticipated in (18) (open black triangle with cross in Fig. 7). In this case, the flow does not stagnate along the valley floor even though $NH/U = -1.4$ (Fig. 7b). The flow, however, retains features of the hydrostatic cases in Figs. 6d and 6e, in which there are internal wave breaking and a tendency to produce a regular series of upstream-propagating waves.

Figures 6e, 6f, and 6i feature upstream-propagating disturbances that we believe are linear waves, because all three cases are subcritical; our guess is that the waves are produced by the nonlinear flows in the valley.

Figure 6j is an example of the extremely complex behavior that can be realized in this ostensibly simple flow situation (filled black circle with cross in Fig. 7). As indicated in Fig. 7c, the flow is well into the stagnant, subcritical regime. As expected for the subcritical case, there is the propensity for internal wave breaking, but at the same time there is also flow stagnation in the valley. The result is the flow shown in Fig. 6j, in which the lower branch of the approaching stratified flow decouples from the flow above it, undergoes a jumplike feature as it encounters the stagnant cold pool, and continues downstream with a series of apparently nonhydrostatic waves superimposed. While we have no definitive explanation for the latter, we can offer the following speculation: a hydraulic jump in a single layer is sometimes followed by a train of waves that, according to Benjamin and Lighthill (1954), allow momentum, energy, and mass conservation across the jump [in the classical case (Rayleigh 1914), there are no waves, momentum and mass are conserved, and energy is dissipated]. It appears that the nonlinearity in the valley in this case

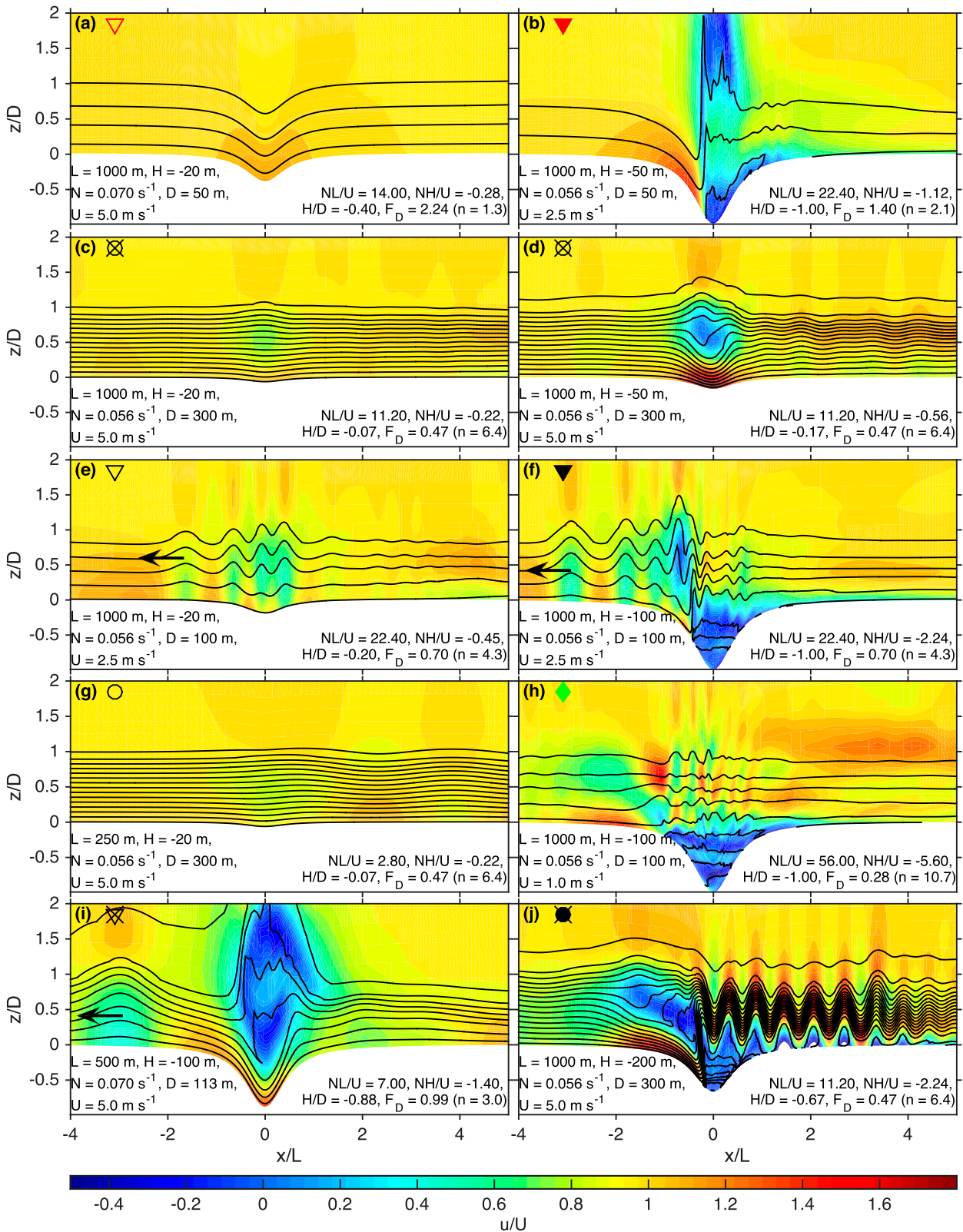


FIG. 6. Examples of solutions in the different flow regimes illustrated by cross sections of u/U (colors) and potential temperature (black isolines). The simulation parameters and regime-indicator icons are shown in each panel. Each example is indicated in the regime diagram in Fig. 7.

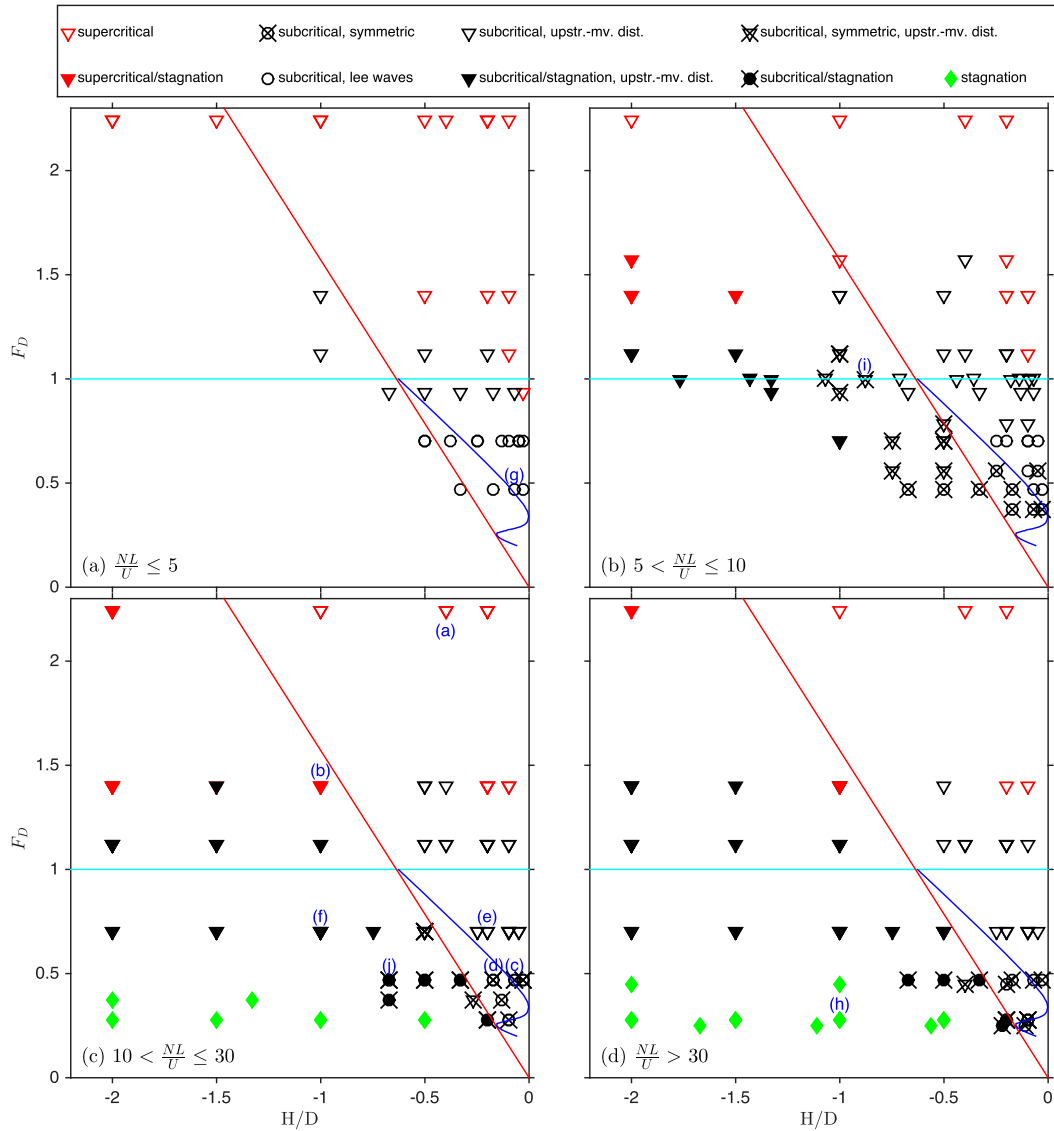


FIG. 7. Regime diagram for the set of simulations listed in Table 1 following Fig. 5, but with an expanded range of F_D and H/D and for (a) $NL/U \leq 5$, (b) $5 < NL/U \leq 10$, (c) $10 < NL/U \leq 30$, and (d) $NL/U > 30$. The open symbols define solutions with no flow stagnation; the filled symbols indicate stagnation either within or above the valley. Symbols with \times running through them indicate solutions with a wind speed dipole over the valley with a maximum at the surface and a minimum aloft; wave breaking can occur within the wind minimum. Red (black) symbols indicate supercritical (subcritical) upstream conditions; the green symbols indicate nearly total valley-flow stagnation.

splits the lower layer in two, with the lower part acting like the single layer described by Benjamin and Lighthill (1954).

Finally two general points about Fig. 7 can be made. First, consistent with (18), flows without valley stagnation can occur for $NH/U < -1$ and for F_D ranging from below to above unity in cases of smaller NL/U . Second, flows categorized as “subcritical/stagnation, upstreaming-moving disturbances,” such as that in Fig. 6f, can occur for $F_D > 1$, which indicates an effect on the upstream

environment that would allow upstream wave propagation in violation of (7).

5. Summary

The present study is motivated by the flow conditions typical of the Arizona Meteor Crater (Fig. 1) and by the related idealized modeling study by the authors (Lehner et al. 2016b). It was found in the latter study that the response of a thermally generated slope flow to the

presence of an embedded two-dimensional crater (i.e., a valley) can largely be understood in terms of the inviscid fluid dynamics of stratified flow.

The observed and modeled stratification suggests a two-layer idealization with constant stratification in the lower layer and zero stratification above; with the further idealization of a height-independent ambient flow, we have the simplest nontrivial relevant flow. The idealization, shown schematically in Fig. 2, has three input parameters (N , D , and U) characterizing the upstream flow and two that describe the valley (H and L). Dimensional analysis indicates that the solution for the steady-state flow can depend on at most three nondimensional combinations of the five dimensional inputs. Numerical results are presented in terms of NH/U , NL/U , $F_D = \pi U/(2ND)$, and H/D for a wide range of these parameters.

A significant advantage of the present flow idealization is that there are well-developed linear and nonlinear theories for the flow response to topography. A major component of the present work is the review of these theories and the further exploration of the nonlinear theory for flow over a valley, which has received much less emphasis in the literature with respect to a hill. The nonlinear Long's theory predicts accelerated flow in the valley with no critical-flow transitions for $F_D > 1$. For $F_D < 1$, the nonlinear theory allows critical-flow transitions, but in many cases they cannot be realized, as the predicted flow has internal flow reversal (dashed line in Fig. 3) that invalidates the assumptions on which the theory relies. Despite the technical invalidity of the solutions in this range, the threshold solution behavior suggests how to interpret the numerical results that lie outside the theoretical range of validity. Finally, new heuristic arguments are advanced to explain the conditions under which flow stagnation is expected in the valley.

The results of the present numerical investigation are summarized in the regime diagram Fig. 7 along with the examples of each flow type in Fig. 6. The major results are as follows:

- For $F_D > 1$ and $NH/U > -1$, symmetric valley flow occurs over a wide range of NL/U , with no upstream waves.
- For $F_D > 1$ and $NH/U < -1$, stagnant valley flow occurs for $NL/U \geq 10$, with no upstream waves.
- For $F_D < 1$ and $NH/U > -1$, Long's theory and simulations indicate surface flow acceleration and midlayer

flow deceleration; however, for values of F_D closer to unity, upstream-propagating short waves are produced in the valley.

- For $F_D < 1$ and $NH/U < -1$, valley-flow stagnation and/or internal wave breaking occurs except for $NL/U < 5$.

Acknowledgments. M. Lehner's contribution to this research was supported by NSF's Physical and Dynamic Meteorology Division through Grant AGS-1160730.

REFERENCES

- Baines, P. G., 1995: *Topographic Effects in Stratified Flow*. Cambridge University Press, 482 pp.
- , and H. Granek, 1990: Hydraulic models of deep stratified flows over topography. *The Physical Oceanography of Sea Straights*, L. J. Pratt, Ed., NATO ASI Series, Vol. 318, Kluwer, 245–269, doi:10.1007/978-94-009-0677-8_12.
- Benjamin, T. B., and M. Lighthill, 1954: On cnoidal waves and bores. *Proc. Roy. Soc. London*, **224A**, 448–460, doi:10.1098/rspa.1954.0172.
- Bryan, G. H., and J. M. Fritsch, 2002: A benchmark simulation for moist nonhydrostatic numerical models. *Mon. Wea. Rev.*, **130**, 2917–2928, doi:10.1175/1520-0493(2002)130<2917:ABSFMN>2.0.CO;2.
- Durrant, D. R., and J. B. Klemp, 1987: Another look at downslope winds. Part II: Nonlinear amplification beneath wave-overturning layers. *J. Atmos. Sci.*, **44**, 3402–3412, doi:10.1175/1520-0469(1987)044<3402:ALADWP>2.0.CO;2.
- Kimura, F., and P. Manins, 1988: Blocking in periodic valleys. *Bound.-Layer Meteor.*, **44**, 137–169, doi:10.1007/BF00117296.
- Lehner, M., and Coauthors, 2016a: The METCRAX II field experiment: A study of downslope windstorm-type flows in Arizona's Meteor Crater. *Bull. Amer. Meteor. Soc.*, **97**, 215–235, doi:10.1175/BAMS-D-14-00238.1.
- , R. Rotunno, and C. D. Whiteman, 2016b: Flow regimes over a basin induced by upstream katabatic flows—An idealized modeling study. *J. Atmos. Sci.*, **73**, 3821–3842, doi:10.1175/JAS-D-16-0114.1.
- Long, R. R., 1953: Some aspects of the flow of stratified fluids. I. A theoretical investigation. *Tellus*, **5A**, 42–58, doi:10.1111/j.2153-3490.1953.tb01035.x.
- Ogura, Y., and N. A. Phillips, 1962: Scale analysis of deep and shallow convection in the atmosphere. *J. Atmos. Sci.*, **19**, 173–179, doi:10.1175/1520-0469(1962)019<0173:SAODAS>2.0.CO;2.
- Rayleigh, L., 1914: On the theory of long waves and bores. *Proc. Roy. Soc. London*, **90A**, 324–328, doi:10.1098/rspa.1914.0055.
- Smith, R. B., 1985: On severe downslope windstorms. *J. Atmos. Sci.*, **42**, 2597–2603, doi:10.1175/1520-0469(1985)042<2597:OSDW>2.0.CO;2.
- Yih, C.-S., 1965: *Dynamics of Nonhomogeneous Fluids*. Macmillan, 306 pp.